Quantum Electronics **51** (1) 64–72 (2021)

https://doi.org/10.1070/QEL17487

Prospects for using silicon nanoparticles fabricated by laser ablation in hyperthermia of tumours

O.I. Sokolovskaya, S.V. Zabotnov, L.A. Golovan, P.K. Kashkarov, D.A. Kurakina, E.A. Sergeeva, M.Yu. Kirillin

Abstract. **The efficiency of using silicon nanoparticles, produced by laser ablation of porous silicon in liquids, as agents for hyperthermia of tumours using laser radiation with wavelengths of 633 and 800 nm is evaluated. Using the optical parameters of the nanoparticles suspensions determined earlier by the spectrophotometry measurements, the heating of tumour tissue with embedded nanoparticles is numerically modelled. The heat transfer equation is solved by the finite element method which considers the volumetric distribution of the absorbed light power, calculated by the Monte Carlo technique, as a distributed heat source. The simulations performed indicate that embedding silicon nanoparticles with a concentration of up to 5 mg mL^{-1} into a tumour allows its maximum temperature to be increased by 0.2–4 °C in comparison with heating the tumour without nanoparticles depending on the irradiation wavelength and intensity.**

Keywords: *pulsed laser ablation in a liquid, light scattering, Monte Carlo technique, finite elements method, hyperthermia.*

1. Introduction

Hyperthermia is a tumour therapy approach consisting in heating a tumour to temperatures in the range of 41–45 °C, which causes irreversible functional changes, including blood supply disorders and death of malignant cells [1–5]. The localisation of the temperature increase exclusively in the tumour is key for hyperthermia, since it allows avoiding negative impact on the surrounding healthy tissues [6, 7]. The use of optical radiation is a promising solution to this problem: the impact localisation and targeting are provided owing to possibilities for configuration of the irradiation beam profile and focusing only in the tumour region. Additionally, targeting can be ensured by direct injection or accumulation of nanoparticles with a large absorption cross section in tumour [8].

O.I. Sokolovskaya, S.V. Zabotnov, L.A. Golovan, P.K. Kashkarov Faculty of Physics, Lomonosov Moscow State University, Leninskie Gory 1, 119991 Moscow, Russia;
e-mail: oi.sokolovskaja@physics.msu.ru;
D.A. Kurakina, M.Yu. Kirillin Institute of Applied Physics, Russian Academy of Sciences, ul. Ul'yanova 46, 603950 Nizhny Novgorod, Russia; e-mail: mkirillin@yandex.ru;
E.A. Sergeeva Institute of Applied Physics, Russian Academy of Sciences, ul. Ul'yanova 46, 603950 Nizhny Novgorod, Russia; Faculty of Physics, Lomonosov Moscow State University, Leninskie Gory 1, 119991 Moscow, Russia

Received 24 November 2020
Kvantovaya Elektronika **51** (1) 64–72 (2021)
Translated by M.Yu. Kirillin

Hyperthermia of biological tissues using nanoparticles of various shapes and their combinations as agents for local enhancement of absorption has been actively discussed recently [9–14]. The requirement for embedding the nanoparticles into biotissue and their subsequent biodegradation limit the nanoparticle size down to 100 nm [15, 16]. Traditionally such nanoparticles are fabricated from substances with high absorption in the diagnostic transparency window of biotissues: carbon, gold, silver, silicon, and iron [17, 18], which provides a high absorption contrast and localisation of the required heat.

However, for successful therapeutic use of hyperthermia, it is extremely important that the indicated nanoparticles were biocompatible and biodegradable. In this connection, the use of silicon nanoparticles (SNPs) as agents for hyperthermia, which are effectively released from the body by dissociation to orthosilicic acid – a natural compound for the human body [19, 20], has a high potential. The SNPs fabricated with the use of porous silicon are of special interest, since this substance is formed by silicon nanocrystals with a size of 2–5 nm (microporous silicon, MCPS) or 5–50 nm (mesoporous silicon, MSPS) separated by pores with dimensions comparable to the sizes of nanocrystals. This material can be produced using electro-chemical etching of monocrystalline silicon plates in an electrolyte containing fluorine ions. At the same time, the sizes of pores and nanocrystals will be primarily determined by etching conditions (electrolyte composition, etching current density) and the initial plates doping degree (as a rule, mesoporous silicon layers are formed on heavily doped substrates, while for microporous ones moderately doped substrates are employed) [21, 22]. To obtain nanoparticles suitable for further use in biomedicine, the manufactured layers of porous silicon are subjected to additional mechanical grinding [23–27] or ultrasonic grinding [28–33], which, however, in most cases does not allow obtaining particles with an average particle size less than 100 nm. Until now, the efficiency of tumour hyperthermia with embedding SNPs fabricated of porous silicon was demonstrated for heating with ultrasound [23], radiofrequency [24], and near-infrared [29, 30] irradiation. However, these studies were performed for relatively large nanoparticles with an average size of at least 100 nm, for which a significant problem of targeted delivery remains open.

An alternative technique for fabricating SNPs is the technique of pulsed laser ablation in liquids allowing one to manufacture SNPs with sizes of tens of nanometres with a high degree of chemical purity [34–38] suitable for biological applications. Using porous silicon as targets for ablation allows the threshold of this process to be significantly lowered

in comparison with the case of ablation of crystalline silicon [39] due to the smaller thermal conductivity of the porous matrix as compared to a bulk material and destruction of Si–Si bonds in the crystal lattice during electrochemical etching. As a result, it leads to a significant increase in the mass outcome of SNPs with the same energy characteristics of laser radiation.

Recently it has been shown that under irradiation of unicellular organisms of *Paramecium Caudatum* suspended in an aqueous suspension with a focused laser beam with a wavelength of 808 nm and an intensity of 15 kW cm^{-2} the addition of SNPs with sizes less than 50 nm manufactured by laser ablation of crystalline silicon leads to an increase in heating compared to the case without nanoparticles (for up to 2.5 °C) and to cell death upon the corresponding increase in temperature [37]. In the same work a numerical simulation of heating was performed for SNPs suspended in water without living organisms for the beam parameters used in the experiment, which showed the fundamental possibility of heating such suspensions in the focus of the laser beam from 30 °C to temperatures exceeding 55 °C. At the same time, the description of hyperthermia of real biological tissues, including both tumours and healthy tissues, requires accounting for their absorption, scattering, and thermal conductivity properties. It should be noted that in works on photohyperthermia using SNPs produced by ultrasound grinding of porous silicon matrices [29, 30], only empirical data on the impact of non-monochromatic light in the wavelength range of 780–1400 nm for cells and tumours in tissues are considered without an analysis of the effect of these properties on the efficiency the considered therapy approach. In this regard, the simulation of heating of biotissues with embedded SNPs with continuous laser radiation is of importance, since such a study would allow assessing the possibility of application of SNPs less than 100 nm in size in photohyperthermia. An additional advantage of the considered nanoparticles consists in their potential use as contrast agents in non-invasive imaging modalities [26, 34, 38, 39], which will allow controlling the targeted delivery of SNPs before the procedure, thus implementing the principles of theranostics: performance of diagnostics and therapy with the same agents.

In this paper, a numerical simulation of heating of a biotissue model by a continuous-wave laser radiation was performed for different wavelengths and intensities. The biotissue model is represented by a two-layer medium, in which the top layer mimics normal human skin, and the lower one mimics a tumour with embedded SNPs with typical size less than 100 nm fabricated by laser ablation of porous silicon films in water and ethanol.

2. Methods and materials

In this work, a numerical simulation of the process of heating a tumour with embedded SNPs with radiation of a continuous-wave laser is reported for two wavelengths, 633 and 800 nm, located within the biotissues transparency window (600–1300 nm), which provides radiation penetration depth in biological tissue of the order of units of millimetres. The radiation intensity was varied in the range of 100–500 mW cm^{-2}, for which, according to the Letokhov scheme [40], a biotissue is only heated, which excludes more significant effects, for example, tissue thermal destruction. Moreover, the intensities of this range are widely used in photodynamic therapy and provide heating to temperatures not exceeding or insignificantly exceeding 42 °C (see, for example, [41, 42]). The irradiation area of the laser beam on the tissue surface was assumed to have the square shape with an area of 1 cm^2 with uniform intensity distribution, which can be achieved with typical laser radiation homogenisers (see, for example, [43]). The simulation was performed for several types of SNPs, the parameters of which correspond to the SNPs formed by picosecond laser ablation of porous silicon films in water and ethanol, described in detail in paper [38]. For all selected types, the SNP average diameter ranged from 14 to 65 nm.

For calculations, the object under study was represented by a two-layer medium mimicking biotissue: the parameters of the upper layer correspond to those of normal human skin, while for the lower one they correspond to a subcutaneous tumour (Fig. 1). In this study the case of targeted delivery of SNPs to the tumour is considered. In the model employed, it is assumed that after the SNPs are administered into biotissue, they are contained only in the lower layer of the medium corresponding to the tumour. The skin layer thickness was considered equal to 0.2 mm (which corresponds to the typical thickness of human epidermis), while the thickness of the entire sample was 10 mm. In transverse section, the considered medium is a square with a size of 51 × 51 mm.

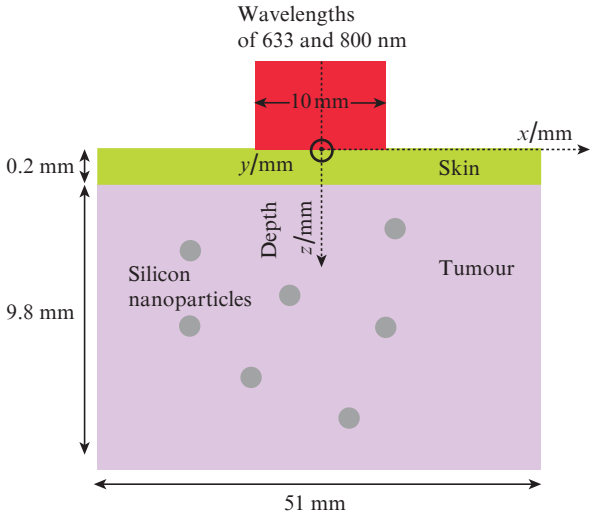

Figure 1. Biotissue model employed in the numerical experiment.

The optical properties of the upper and lower layers of the biotissue model at two considered wavelengths correspond to those of human skin and basal cell carcinoma [44] and are presented in Table 1.

Table 1. Optical properties of biotissue model layers for wavelengths of 633 and 800 nm [44].

Layer	λ = 633 nm			λ = 800 nm		
	μ_a/cm^{-1}	μ_t/cm^{-1}	g	μ_a/cm^{-1}	μ_t/cm^{-1}	g
Skin	2.5	177.5	0.8	1.9	136.9	0.8
Tumour	1.7	151.7	0.8	0.9	100.9	0.8

The values of the optical parameters of the SNPs were chosen in agreement with the results reported in paper [38]. The values of absorption coefficient factors μ_a and extinction coefficient $\mu_t = \mu_a + \mu_s$ (where μ_s is the scattering coefficient), as well as anisotropy factor g for the fabricated SNP suspensions were reconstructed by analysing of the measured spectra of collimated transmittance, diffuse transmittance, and reflectance using the inverse Monte Carlo technique [45] and are presented in Table 2.

Table 2. Optical parameters of SNP suspensions fabricated by laser ablation of porous silicon in liquids, and average sizes of SNPs [36].

Wavelength/ nm	Target type and buffer liquid for ablation	μ_a/cm^{-1}	μ_t/cm^{-1}	g	SNP mean size and dispersion/ nm
633	MCPS in water	0.078	1.03	0.30	65±22
	MCPS in ethanol	0.201	1.12	0.31	28±22
	MCPS in water	0.586	2.32	0.19	14±10
	MCPS in ethanol	0.371	2.72	0.40	25±13
800	MCPS in water	0.040	1.35	0.38	65±22
	MCPS in ethanol	0.009	0.60	0.34	28±22
	MCPS in water	0.036	0.82	0.03	14±10
	MCPS in ethanol	0.019	1.26	0.36	25±13

In suspensions fabricated by laser ablation in liquids, the main volume is occupied by a buffer liquid: the mass fraction of nanoparticles is ~0.5 mg mL^{-1} [38]. In paper [46] it was demonstrated that for intravenous injection the mass concentration of silicon particles in different organs, including tumour, can reach 0.01%–0.08%, which approximately corresponds to the concentrations of 0.1–0.8 mg mL^{-1}. It should be noted that upon local injection higher concentrations of nanoparticles in tumour can be achieved: in [47], when estimating the effect of hyperthermia, the concentrations of upconversion nanoparticles in the range of 2–9 mg mL^{-1} are considered. In this study, the concentrations of SNPs in the range of 0.31–5.00 mg mL^{-1} are considered. Partial light scattering μ_s^{susp} and absorption μ_a^{susp} coefficients of SNPs in medium are determined as follows:

$$\mu_s^{susp} = \sigma_s^{np} C, \quad \mu_a^{susp} = \sigma_a^{np} C, \tag{1}$$

where σ_s^{np} and σ_a^{np} are the scattering and absorption cross sections of a single SNP; and C is the SNP concentration in the medium. It is assumed that the concentration C^{tum} of SNPs in tumour increases by a multiplicative factor of k with respect to the SNP concentration in the suspension; therefore, the partial scattering and absorption coefficients accounting for scattering and absorption by nanoparticles embedded in the tumour also increase by a factor of k, respectively. In calculations it is assumed that after embedding into the tumour the volume fraction of SNPs remains small, and the scattering and absorption coefficients can be considered as additive quantities [48]. Thus, the tumour is characterised by scattering (μ_s), absorption (μ_a), extinction (μ_t) coefficients, and anisotropy parameter g:

$$\mu_s^{tum+np} = \mu_s^{tum} + k\mu_s^{susp}, \tag{2}$$

$$\mu_a^{tum+np} = \mu_a^{tum} + k\mu_a^{susp}, \tag{3}$$

$$\mu_t^{tum+np} = \mu_s^{tum+np} + \mu_a^{tum+np}, \tag{4}$$

$$g^{tum+np} = \frac{\mu_s^{tum} g^{tum} + k\mu_s^{susp} g^{susp}}{g^{tum} + g^{susp}}, \tag{5}$$

where superscripts 'tum' and 'tum + np' refer to tumour and tumour with embedded nanoparticles, respectively. In calculations, in accordance with the selected concentrations of SNPs in the tumour, k varied from 0.62 to 10. Optical properties of the tumour containing SNPs, calculated within the frames of the assumptions made, are presented in Table 3.

Table 3. Optical properties of tumour with embedded SNPs.

Wavelength/ nm	Target type and buffer liquid for ablation	μ_a/cm^{-1}	μ_t/cm^{-1}	g
633	MCPS in water	2.48	161.95	0.77
	MCPS in ethanol	3.71	162.83	0.77
	MCPS in water	7.56	174.89	0.74
	MCPS in ethanol	5.41	178.88	0.75
800	MCPS in water	1.30	106.76	0.79
	MCPS in ethanol	0.99	106.99	0.77
	MCPS in water	1.26	109.46	0.74
	MCPS in ethanol	1.09	113.70	0.75

Numerical simulation of temperature volumetric distribution in the medium under laser irradiation was performed in two stages. At the first stage, the volumetric distribution of absorbed power (absorption map) in the medium under consideration (Fig. 1) is simulated using the Monte Carlo technique [49–51] for a continuous-wave laser radiation. The principle of this technique consists in calculating a large number of random trajectories of photons in the medium followed by statistical analysis of the data obtained. To increase the efficiency of calculations, when simulating a single trajectory, a photon packet (hereinafter, a photon) is considered instead of a single photon, to which the weight of $W = 1.$ is assigned upon entering the medium. At each iteration step of the algorithm, the photon moves in the medium for a distance

$$s = -\frac{\ln \xi}{\mu_t}, \tag{6}$$

where ξ is a random number in the range (0, 1), in the direction determined by the value of the anisotropy factor and the Henyey–Greenstein phase function. As a result, the photon experiences elastic scattering, which changes the movement direction, and absorption, which causes a photon weight loss proportional to a decrease in photon packet energy:

$$\Delta W = \frac{\mu_a}{\mu_t} W. \tag{7}$$

The computational grid for the absorption map consists of voxels, three-dimensional cells of parallelepiped shape. At each step of calculating the trajectory next node the energy corresponding to the photon weight loss is added to the current value of the absorption map element corresponding to the voxel containing the trajectory node. The ratio of the total energy absorbed in each voxel to the voxel volume is a discrete function of the volumetric density of heat sources $Q_{ext}(x,y,z)$ for the medium, where x, y, and z are the coordinates of voxel centres. The size of the computational grid voxels was $1 \times 1 \times 0.1$ mm.

The simulations were performed for 10^5 photons (the standard deviation of the integral of the absorption map for such statistics amounted to 1%).

At the second stage of simulations, the obtained discrete functions of heat sources $Q_{ext}(x,y,z)$ were used to solve the nonstationary heat transfer equation for biological tissue (Pennes biothermal equation) [52]:

$$\rho C_p \frac{\partial T}{\partial t} - \nabla \times (\kappa \nabla T) = \rho_{bl} C_{bl} \omega_{bl} (T_{bl} - T) + Q_{met} + Q_{ext}, \quad (8)$$

where ρ is the biotissue density; C_p is the biotissue heat capacity at a constant pressure; κ is the thermal conductivity; ρ_{bl}, C_{bl}, T_{bl} and ω_{bl} are the density, the heat capacity, the temperature, and the blood perfusion coefficient (blood transfer through capillaries and extracellular spaces in tissue [53]), respectively; and Q_{met} is the speed of metabolic heat generation the per unit volume [54]. The solution of the Eqn (8) was performed in the COMSOL Multiphysics® software package using the finite element method [55–57]. Boundary conditions were as follows: a constant temperature of 37 °C on the medium surfaces within biotissue, and convection at the skin–air boundary [58]; convective heat transfer coefficient $h = 18$ W m^{-2} K^{-1}, and air temperature was assumed to be 25 °C. The initial temperature of the entire medium was 37 °C, and the blood temperature was $T_{bl} = 37.15$ °C.

The values of the parameters in the heat transfer equation used in the simulations are presented in Table 4.

Table 4. Thermophysical properties of the studied biotissues [59].

Biotissue	C_p/ J kg^{-1} K^{-1}	ρ/ kg m^{-3}	κ/ W m^{-1} K^{-1}	ω_{bl}/s^{-1}	Q_{met}/ W m^{-3}
Skin	2291	1180	0.580	0.0005	420
Tumour	4200	1150	0.561	0.0036	420
Blood	3770	1060	–	–	–

The computational grid employed for the solution of the heat transfer equation corresponded to that used for calculating absorption maps by the Monte Carlo technique.

The modelling performed allowed us to calculate thermal fields in biotissue both for a tumour without SNPs and for tumours with different concentrations of SNPs. The dependence of the temperature depth profile on the radiation power and concentration of nanoparticles in biotissue was studied.

3. Results and discussion

Figure 2 shows the central in-depth sections of the absorption map $Q_{ext}(x = 0, y = 0, z)$, representing dependences of the volumetric density of the absorbed light power along the axis of the incident laser beam on depth z for media without SNPs and with different types of SNPs for irradiation at wavelengths of 633 (Fig. 2a) and 800 nm (Fig. 2b). The results are presented for the maximal considered intensity $I =$ 500 mW cm^{-2}.

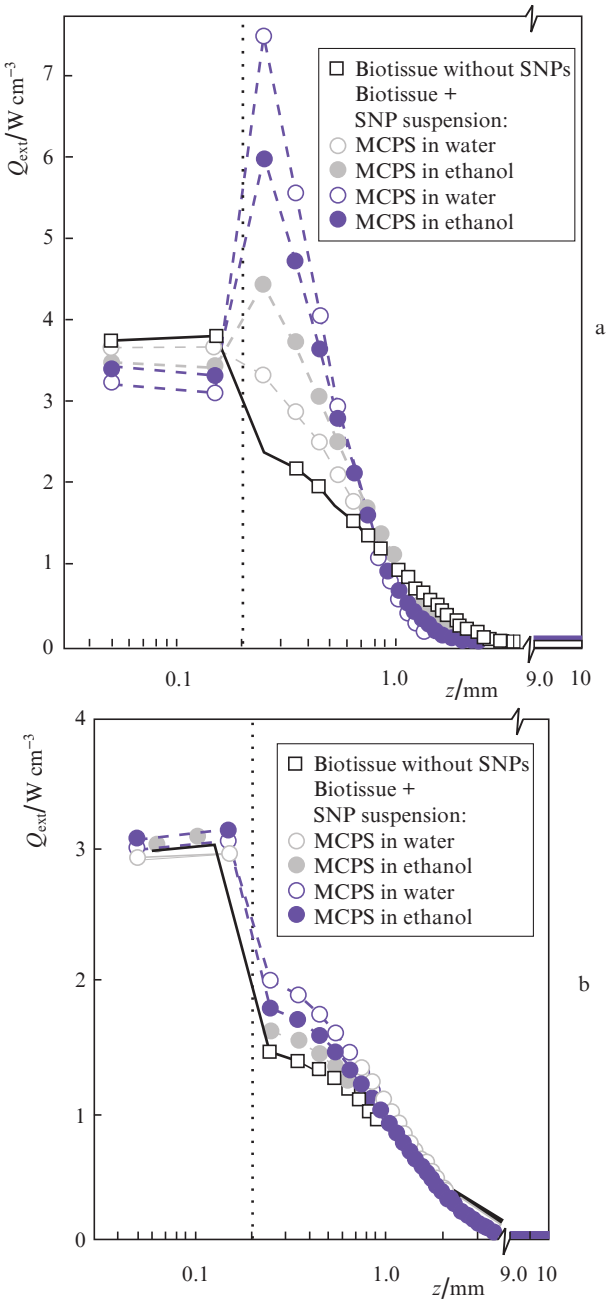

Figure 2. Effect of the embedding of SNPs into the tumour on the in-depth distribution of the volumetric density of the laser radiation power Q_{ext} absorbed by biotissue on the laser beam axis (x, $y = 0$) in a two-layer biological tissue (dashed lines indicate the skin–tumour boundary) upon irradiation with continuous-wave laser radiation with an intensity of 500 mW cm^{-2} at wavelengths of (a) 633 and (b) 800 nm.

The most pronounced changes in the absorbed power density distribution are observed at the skin–tumour boundary (indicated in Fig. 2 by a vertical dashed line), which are caused by the difference in layer optical properties. Absorption of the radiation in both biotissue layers is larger at a wavelength of 633 nm as compared to 800 nm; which is due to the larger value of the biotissue absorption coefficient in the visible range (see Table 1). The addition of SNPs to the lower layer increases its absorption and scattering coefficients (Tables 1 and 3), which leads to an increase in the absorbed power. It is quite expected that embedding SNPs with a higher partial absorption coefficient increases the absorbed power volumetric density. This effect is the most pronounced at a wavelength of 633 nm (Fig. 2a), where SNPs fabricated by ablation of mesoporous silicon in water and ethanol provide a 2- and 3-fold increase in the maximum absorbed power in tumour, respectively, while the in-depth decay of the absorbed power density is also more pronounced for these types of nanoparticles.

Note an accompanying effect consisting in the reduction of the absorbed power in the upper layer caused by increased absorption of radiation in the lower layer resulting in the decrease in the intensity of the backscattered diffuse component arriving to the upper layer from lower one. For SNPs with lower absorption (microporous silicon ablated in water and ethanol), this effect is less pronounced.

Since for a wavelength of 800 nm, the absorption coefficient of both biotissue and SNPs is much smaller than that for 633 nm, the contribution of the backscattered diffuse wave to the absorbed power is not essential in this case, and the embedding of SNPs does not noticeably affect the absorbed power density in the upper layer (Fig. 2b), while an increase in the absorbed power at depths exceeding 0.4 mm in the second layer monotonically depends on the value of the partial absorption coefficient of SNPs.

The largest values of the absorbed power volumetric density in this case are achieved for SNPs fabricated by laser ablation of micro- and mesoporous silicon in water, which determined the selection of these SNP types for further calculations.

Figures 3a and 3b show two-dimensional distributions $Q_{ext}(x, y = 0, z)$ in the medium for irradiation at a wavelength of 633 nm (uniform illumination of the 10 × 10 mm area) for the cases without SNPs in tumour (Fig. 3a) and with the embedded-in-tumour SNPs ablated from mesoporous silicon in water (Fig. 3b). As shown above, embedding the specified SNPs in the tumour layer localises the radiation absorption, while the absorbed radiation power density for I = 500 mW cm^{-2} increases up to three times (Fig. 2 a). Figures 3c and 3d show two-dimensional distributions $Q_{ext}(x, y = 0, z)$ in the medium for irradiation at a wavelength at 800 nm for the cases without SNPs in tumour (Fig. 3c) and with the

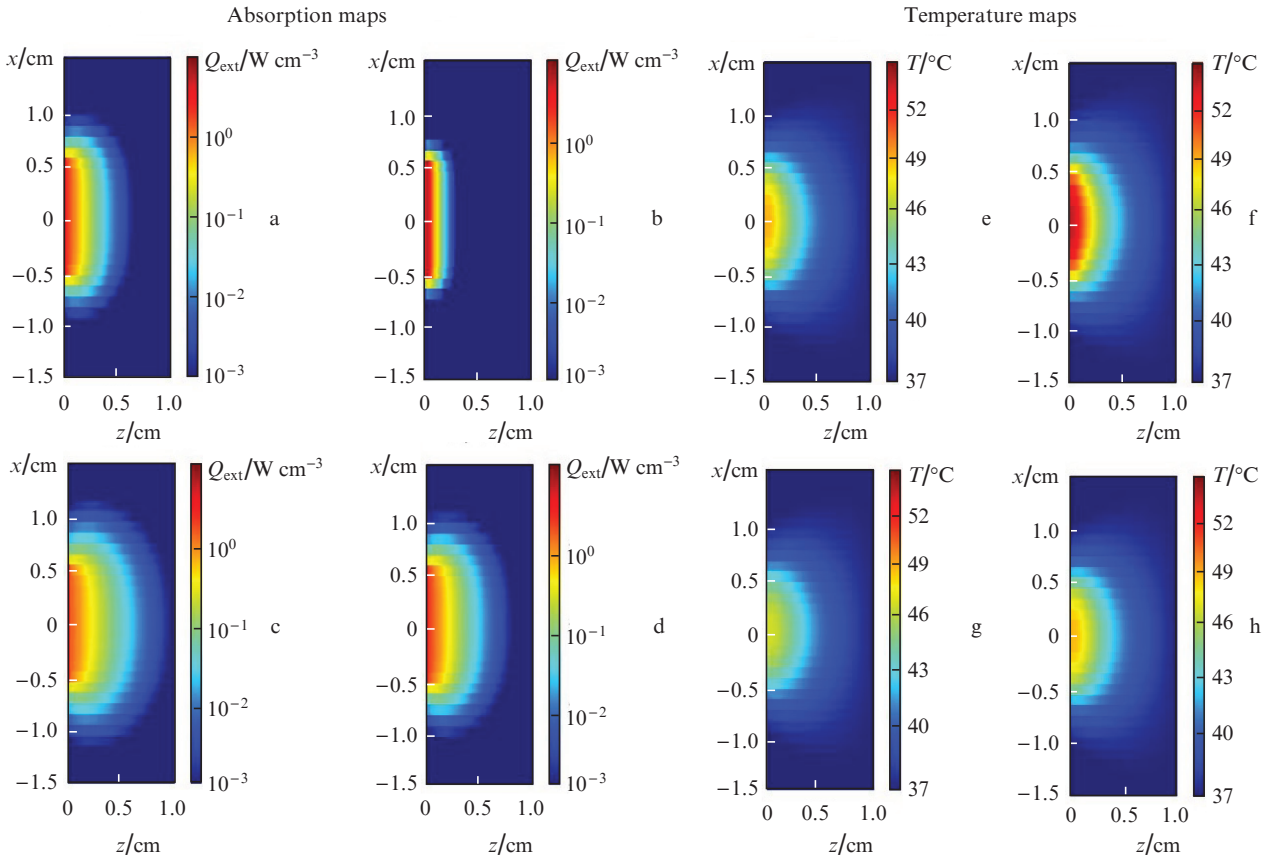

Figure 3. (Colour online) Maps of two-dimensional distributions of the absorbed power density in (a–d) the medium and (e–h) temperature upon irradiation at wavelengths of (a, b, e, f) 633 and (c, d, g, h) 800 nm: (a, c, e, g) without SNPs and (b, d, f, h) in the case of the presence of SNPs fabricated by laser ablation of mesoporous silicon in water in a concentration of 5 mg mL^{-1} in biotissue lower layer. The maps are calculated for irradiation of the medium for 10 min by a beam with a square cross section of 10 × 10 mm with a uniform intensity distribution and intensity of I = 500 mW cm^{-2}.

embedded-in-tumour SNPs ablated from microporous silicon in water (Fig. 3d). For the wavelength of 800 nm the effect of absorption localisation in the tumour layer is significantly weaker, manifested by a small (up to 1.5 times) increase in absorbed energy in the presence of SNPs (Fig. 2b).

For the distributed heat sources calculated by the Monte Carlo technique, the biothermal equation (8) was numerically solved for the two-layer biotissue both with and without embedded SNPs. The calculated temperature distribution maps corresponding to the cases in shown Figs 3a–3d are demonstrated in Figs 3e–3h, respectively.

One can see that for almost all considered regimes, the medium is heated to temperatures in the range of 42–50 °C sufficient for photohyperthermia performance at depths of up to 5 mm.

For a more detailed analysis, Fig. 4 shows the in-depth profiles of temperature field distributions (central sections) for the medium containing SNPs of various types for irradiation at wavelengths of 633 (Fig. 4a) and 800 nm (Fig. 4b) with an intensity of 500 mW cm^{-2}. For the case without SNPs, the heating of biotissue is higher for irradiation at a wavelength of 633 nm due to higher absorption in tumour layer as compared to a wavelength of 800 nm. The presence of SNPs fabricated by ablation of mesoporous silicon in water at a concentration of 5 mg mL^{-1} in the tumour leads to additional heating in comparison with the tumour without SNPs (Figs 4a, 4b): for a wavelength of 633 nm and intensity of 500 mW cm^{-2} the additional temperature increase in ΔT with respect to the case without SNPs is 1–4.2 °C, while for a wavelength of 800 nm it amounts to ΔT = 0.2–1.3 °C. The observed maximum additional heating values provided by the SNPs with the highest absorption coefficients at corresponding wavelengths is quite expected. It should be noted that due to heat transfer in the presence of SNPs, the effect of reducing the absorbed power density in the upper layer at the wavelength of 633 nm does not affect the temperature field, and temperature variations with depth are negligible both in the upper layer and in the lower layer at depths of up to 1 mm, while the increase in temperature is proportional to the partial absorption coefficient of SNPs.

For a more detailed study of the heating process, the kinetics of biotissue heating was calculated at different depths: at the skin–tumour boundary, the skin is a tumour (Figs 5a and 5d), as well as at depths of z = 1 mm (Figs 5b and 5e) and z = 4 mm (Figs 5c and 5f) in the tumour layer. The most essential temperature rise occurs in the first 200 s of irradiation, followed by a significant slowing of the heating rate. For all considered depths, the tendency towards saturation of the local heating was observed after 300 s of irradiation.

Thus, the case of irradiation for 600 s shown in Fig. 4 corresponds to the stationary phase of the considered process. In general, the information on biotissue heating kinetics is useful in developing protocols for performing hyperthermia, more exactly, in working out the recommendations for the optimal exposure time, since an excessive heat can lead to an undesirable heating of the surrounding healthy tissues.

As shown above, embedding of the SNPs from mesoporous silicon ablated in water at a concentration of 5 mg mL^{-1} into the tumour layer upon irradiation with an intensity of 500 mW cm^{-2} leads to the heating of the model object to a temperature of 54 °C (Fig. 4), whereas for the successful

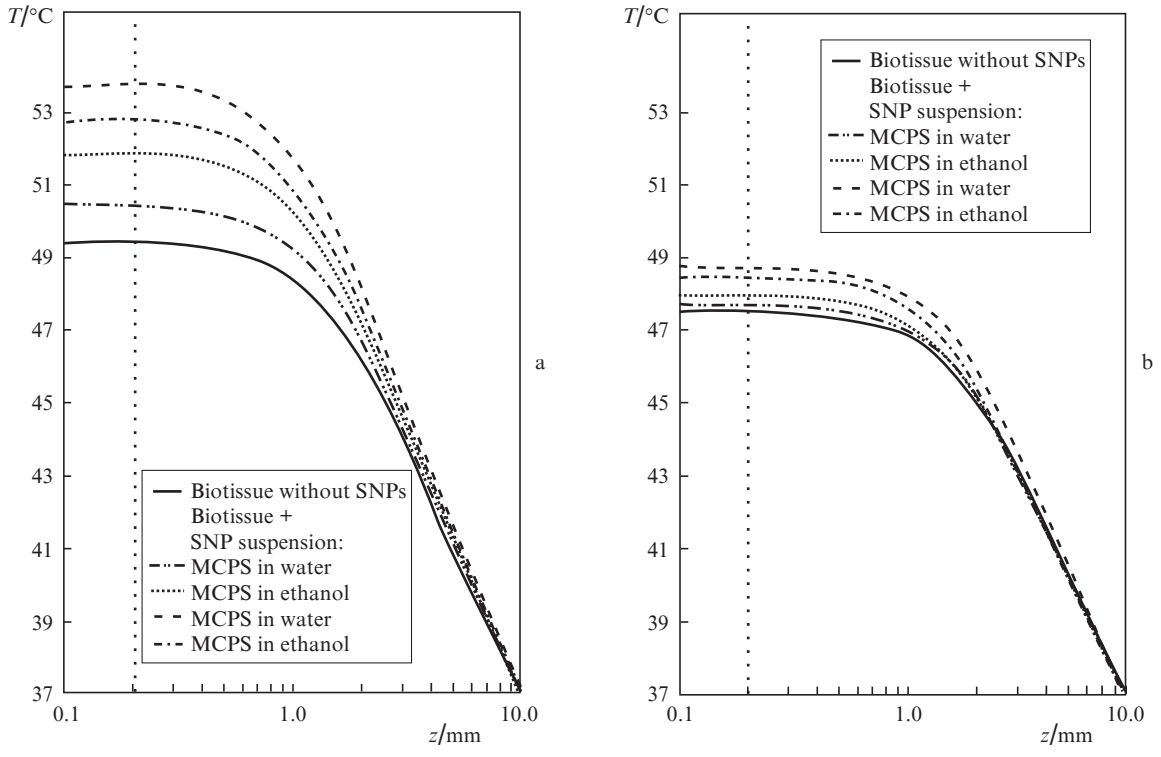

Figure 4. In-depth temperature distribution in the medium without SNPs and in the presence of various types of SNPs in the tumour layer in 600 s after start of irradiation with an intensity of 500 mW cm^{-2} at wavelengths of (a) 633 and (b) 800 nm. Vertical dotted lines indicate skin–tumour boundary.

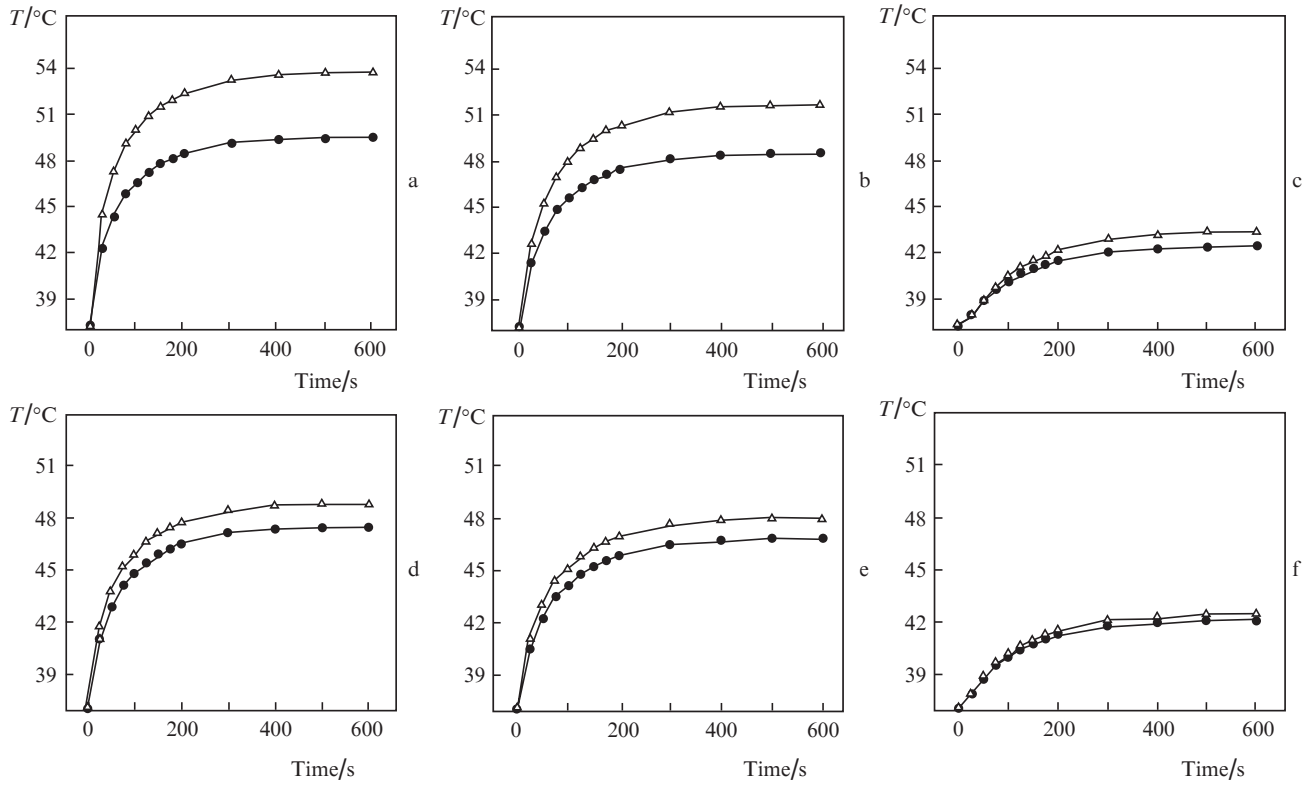

Figure 5. Kinetics of tumour heating without SNPs (●) and in the presence of SNPs (△; 5 mg mL^{-1}) ablated from mesoporous silicon in water at depths of z = (a, d) 0.2, (b, e) 1.0, and (c, f) 4.0 mm for irradiation at wavelengths of (a–c) 633 and (d–f) 800 nm with an intensity of 500 mW cm^{-2}.

implementation of hyperthermia a temperature of ~42 °C is required. Therefore, effective hyperthermia performance is possible at lower irradiation intensities. Additional estimations show that the intensities required for heating the considered medium up to a temperature of 42 °C in the absence of SNPs, are 200 and 250 mW cm^{-2} for irradiation at wavelengths of 633 and 800 nm, respectively.

Figure 6 shows the results of temperature profile simulations for biological tissue without SNPs and with SNPs fabricated by ablation of mesoporous silicon in water in different concentrations upon irradiation of the model medium with I = 200 mW cm^{-2} at a wavelength of 633 nm and with I = 250 mW cm^{-2} at a wavelength of 800 nm. The maximum thickness of the tumour layer L_{42}, in which the condition of hyperthermia is satisfied, i.e. the temperature exceeds 42 °C [6], increases with an increase in the concentration of SNPs in tumour (insets in Fig. 6).

With an increase in the mass concentration of SNPs in tumour from zero to 5 mg mL^{-1} the maximum heating depth L_{42} varies from 0.3 to 1.8 mm for a wavelength of 633 nm and from 0.9 to 1.6 mm for a wavelength of 800 nm. This result indicates that, despite the greater absorption at a wavelength of 633 nm (Table 3) and, accordingly, a smaller depth of radiation penetration into tissue (see Fig. 3), the tumour is heated more effectively as compared to using a laser beam at a wavelength of 800 nm, again, due to a larger absorption of radiation.

Les us consider a point A (x = 0, y = 0, z = 1 mm) within the tumour layer and trace the effect of the radiation intensity and SNPs concentration in the tumour on its temperature. The choice of this point is governed by its location on the beam axis and the maximum depth at which the effective tumour heating is still possible (Fig. 6). Figure 7 shows the isotherms at point A in two coordinates: intensity of laser radiation and concentration of SNPs in the tumour layer.

The same tumour temperature can be achieved at various concentrations of SNPs and radiation intensities. The typical hyperthermia temperature of 42 °C is achieved at concentrations ranging from 0 to 5 mg mL^{-1} and corresponding intensities from 220 to 170 mW cm^{-2} for a wavelength of 633 nm (Fig. 7a) and from 255 to 225 mW cm^{-2} for a wavelength of 800 nm (Fig. 7b). This result fully confirms the appropriate choice of the intensities range employed for calculation of the in-depth temperature distributions shown in Fig. 6.

It is worth mentioning that the obtained estimates of the heating values are in good agreement with the results of other works on monitoring biological tissue temperature upon heating by optical radiation with close parameters. In paper [41] the heating of a rabbit ear ranged from 3.5 to 8 °C upon irradiation at a wavelength of 660 nm with intensity of 200 mW cm^{-2} for the full light dose of 50–100 J cm^{-2}. Note that the thermal conductivity of a rabbit ear and its thickness (about 1 mm) are smaller in comparison with the considered biotissue, which leads to greater heating as compared to the estimates obtained in this study. The results of temperature monitoring of photodynamic therapy of basal cell carcinoma in paper [42] showed that the temperature of biotissue during irradiation at a wavelength of 660 nm with an intensity of 300 mW cm^{-2} for 480 s reached 42 °C, which is also in good agreement with the results obtained in our study for a close wavelength (633 nm).

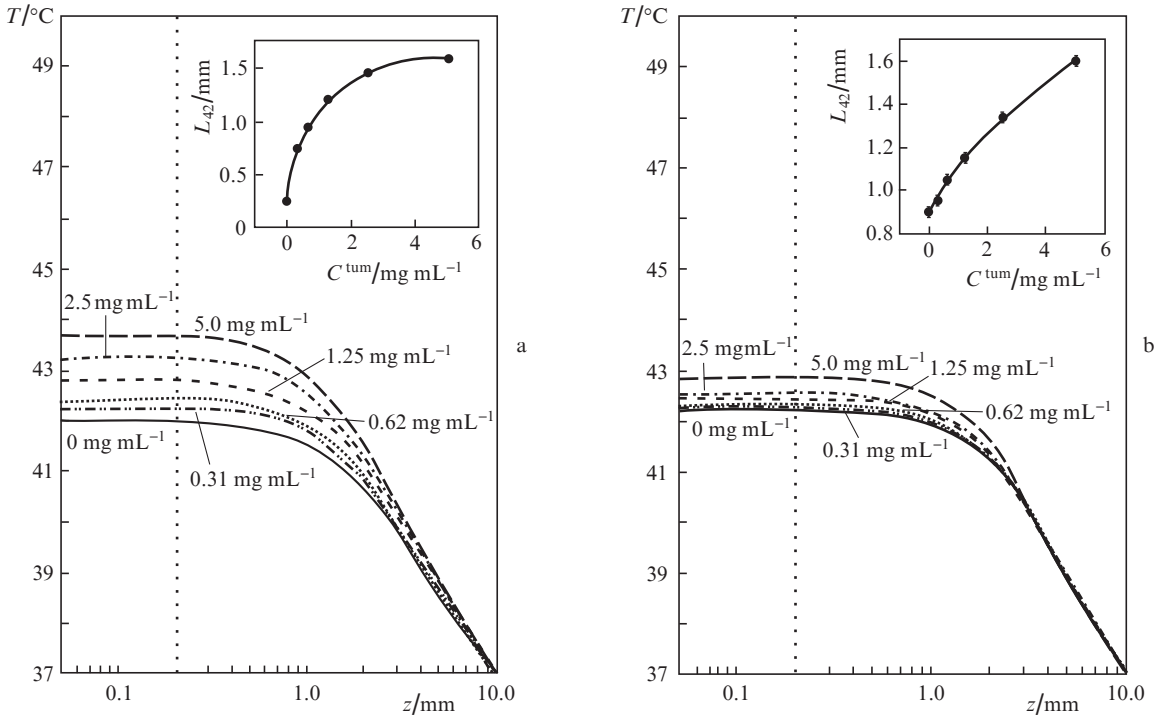

Figure 6. Profiles of in-depth temperature distribution in the model medium at different concentrations of SNPs fabricated by laser ablation of mesoporous silicon in water in a tumour under irradiation (a) at a wavelength of 633 nm with an intensity of 200 mW cm^{-2} and (b) at a wavelength of 800 nm with an intensity of 250 mW cm^{-2}. The corresponding insets show the dependences of the maximum depth L_{42}, where the temperature exceeds 42 °C, on the concentration of SNPs in the lower layer. The error indicated in the inserts is equal to half size of the voxel in the z direction.

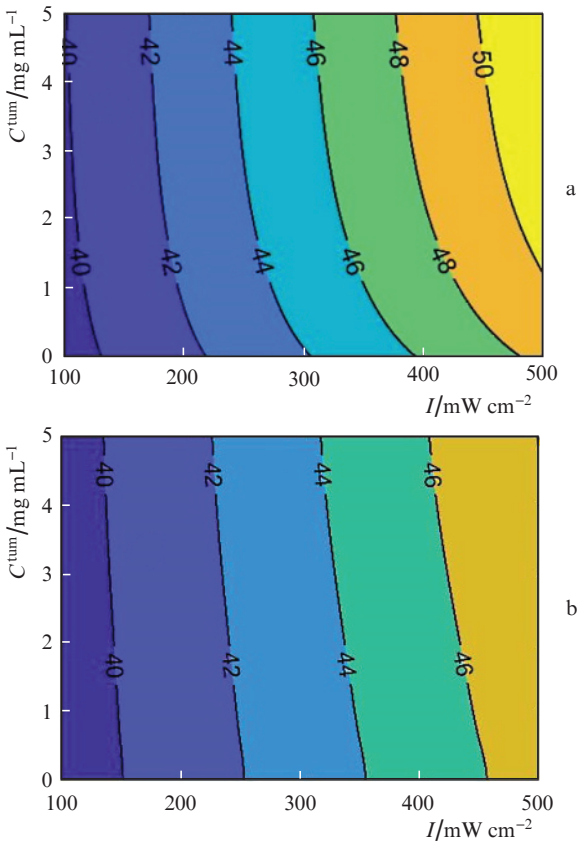

Figure 7. Biotissue heating isotherms at point A (0, 0, 1 mm) for various concentrations of SNPs in tumour and intensities of laser radiation for wavelengths of (a) 633 and (b) 800 nm.

4. Conclusions

In this paper, the Monte Carlo technique and finite elements method were employed for calculating absorption maps and solving the nonstationary heat transfer equation, respectively, to perform numerical simulations of heating of a two-layer medium mimicking a biotissue. The simulation results show that silicon nanoparticles fabricated by picosecond laser ablation of micro- and mesoporous silicon in water and ethanol are promising for photohyperthermia of tumours. The presence of SNPs in biotissue increases the absorption of continuous-wave laser radiation at wavelengths of 633 and 800 nm at depths of up to 1 mm. An additional temperature increase of 0.2–4 °C in the tumour with respect to the tumour without SNPs was demonstrated depending on the wavelength and the intensity of laser radiation, as well as on the target type employed in SNPs fabrication by the laser ablation technique. The largest tumour heating is achieved with embedding SNPs with the maximum absorption at the corresponding wavelengths: SNPs fabricated by ablation of mesoporous silicon in water (for irradiation at a wavelength of 633 nm) and SNPs fabricated by ablation of both meso- and microporous silicon in water (for irradiation at a wavelength of 800 nm). Numerical simulations showed that the temperatures of hyperthermia performance (~42 °C) can be achieved with continuous-wave laser radiation with the intensities of 200 and 250 mW cm^{-2} for the wavelengths of 633 and 800 nm, respectively. Embedding SNPs with concentration of 5 mg mL^{-1} into the tumour layer for irradiation with continuous-wave laser irradiation at a wavelength of 633 nm with intensity of 200 mW cm^{-2} increases the depth of hyperthermia effect on the tumour from 0.3 to 1.8 mm.

Acknowledgements. This work was supported by the Russian Science Foundation (Grant No. 19-12-00192).

References

1. Song C.W., Kang M.S., Rhee J.G., Levitt S.H. *Br. J. Cancer*, **41** (2), 309 (1980).
2. Fuller K.J., Issels R.D., Slosman D.O., Guillet J.-G., Soussi T., Polla B.S. *Eur. J. Cancer*, **30** (12), 1884 (1994).
3. Harmon B.V., Takano Y.S., Winterford C.M., Gobe G.C. *Int. J. Radiat. Biol*., **59** (2), 489 (1991).
4. Abe M., Hiraoka M. *Int. J. Radiat. Biol. Relat. Stud. Physics, Chem. Med*., **47** (4), 347 (1985).
5. Kim J.H., Hahn E.W. *Cancer Res*., **39** (6), 2258 (1979).
6. Chatterjee D.K., Diagaradjane P., Krishnan S. *Ther. Deliv.*, **2** (8), 1001 (2011).
7. Jha S., Sharma P.K., Malviya R. *Achiev. Life Sci*., **10** (2), 161 (2016).
8. Nomura S., Morimoto Y., Tsujimoto H., Arake M., Harada M., Saitoh D., Hara I., Ozeki E., Satoh A., Takayama E., Hase K., Kishi Y., Ueno H. *Sci. Rep*., **10** (1), 1 (2020).
9. Behnam M.A., Emami F., Sobhani Z., Koohi-Hosseinabadi O., Dehghanian A.R., Zebarjad S.M., Moghim M.H., Oryan A. *Adv. Pharm. Bull*., **8** (1), 49 (2018).
10. Behnam M.A., Emami F., Sobhani Z., Dehghanian A.R. *Iran. J. Basic Med. Sci*., **21** (11), 1133 (2018).
11. Norouzi H., Khoshgard K., Akbarzadeh F. *Lasers Med. Sci*., **33** (4), 917 (2018).
12. Cherukuri P., Glazer E.S., Curley S.A. *Adv. Drug Deliv. Rev*., **62** (3), 339 (2010).
13. Tolstik E., Osminkina L.A., Matthäus C., Burkhardt M., Tsurikov K.E., Natashina U.A., Timoshenko V.Yu., Heintzmann R., Popp J., Sivakov V. *Nanomed. Nanotechnol., Biol. Med*., **12** (7), 1931 (2016).
14. Vervald A.M., Burikov S.A., Scherbakov A.M., Kudryavtsev O.S., Kalyagina N.A., Vlasov I.I., Ekimov E.A., Dolenko T.A. *ACS Biomater. Sci. Eng*., **6** (8), 4446 (2020).
15. Howard G.P., Verma G., Ke X., Thayer W.M., Hamerly T., Baxter V.K., Lee J.E., Dinglasan R.R, Mao H.-Q. *Nano Res*., **12**, 837 (2019).
16. De Jong W.H., Hagens W.I., Krystek P., Burger M.C., Sips A.J., Geertsma R.E. *Biomaterials*, **29** (12), 1912 (2008).
17. Adabi M., Naghibzadeh M., Adabi M., Zarrinfard M.A., Esnaashari S.S., Seifalian A.M., Faridi-Majidi R., Tanimowo Aiyelabegan H., Ghanbari H. *Artif. Cells, Nanomed. Biotechnol*., **45** (4), 833 (2017).
18. Skandalakis G.P., Rivera D.R., Rizea C.D., Bouras A., Jesu Raj J.G., Bozec D., Hadjipanayis C.G. *Int. J. Hyperth*., **37** (2), 3 (2020).
19. Ksenofontova O.I., Vasin A.V., Egorov V.V., et al. *Tech. Phys. J*., **59** (1), 66 (2014) [*Zh. Tekh. Fiz*., **84** (1), 67 (2014)].
20. Park Y., Yoo J., Kang M.-H., Kwon W., Joo J. *J. Mater. Chem. B*, **7** (41), 6271 (2019).
21. Bisi O., Ossicini S., Pavesi L. *Surf. Sci. Rep*., **38** (1), 1 (2000).
22. Pavesi L. *La Riv. del Nuovo Cim*., **20** (10), 1 (1997).
23. Sviridov A.P., Andreev V.G., Ivanova E.M., Osminkina L.A., Tamarov K.P., Timoshenko V.Y. *Appl. Phys. Lett*., **103** (19), 193110 (2013).
24. Tamarov K.P., Osminkina L.A., Zinovyev S.V., Maximova K.A., Kargina J.V., Gongalsky M.B., Ryabchikov Y., Al-Kattan A., Sviridov A.P., Sentis M., Ivanov A.V., Nikiforov V.N., Kabashin A.V., Timoshenko V.Yu. *Sci. Rep*., **4** (1), 1 (2014).
25. Sviridov A.P., Osminkina L.A., Kharin A.Yu., Gongalsky M.B., Kargina J.V., Kudryavtsev A.A., Bezsudnova Yu.I, Perova T.S., Geloen A., Lysenko V., Timoshenko V.Yu. *Nanotechnol.*, **28** (10), 105102 (2017).
26. Zabotnov S.V., Kashaev F.V., Shuleiko D.V., et al. *Quantum Electron*., **47** (7), 638 (2017) [*Kvantovaya Elektron*., **47** (7), 638 (2017)].
27. Osminkina L.A., Tamarov K.P., Sviridov A.P., Galkin R.A., Gongalsky M.B., Solovyev V.V., Kudryavtsev A.A., Timoshenko V.Yu. *J. Biophoton.*, **5** (7), 529 (2012).
28. Park J.-H., Gu L., von Maltzahn G., Ruoslahti E., Bhatia S.N., Sailor M.J. *Nature Mater.*, **8**, 331 (2009).
29. Lee C., Kim H., Hong C., Kim M., et al. *J. Mater. Chem*., **18** (40), 4790 (2008).
30. Hong C., Lee J., Zheng H., Hong S.-S., Lee C. *Nanoscale Res. Lett*., **6** (1), 321 (2011).
31. Chaix A., Cheikh K.E., Bouffard E., Maynadier M., Aggad D., Stojanovic V., Knezevic N., Garcia M., Maillard P., Morère A., Gary-Bobo M., Raehm L., Richeter S., Durand J.-O., Cunin F. *J. Mater. Chem. B*, **4**, (21), 3639 (2016).
32. Belamie E., Maillard P., Sailor M.J., Garcia M., Durandad J.-O., Cunin F. *Chem. Commun*., **49** (39), 4202 (2013).
33. Xiao L., Gu L., Howell S.B., Sailor M.J. *ACS Nano*, **5** (5), 3651 (2011).
34. Zabotnov S.V., Kurakina D.A., Kashaev F.V., et al. *Quantum Electron*, **50** (1), 69 (2020) [*Kvantovaya Elektron*., **50** (1), 69 (2020)].
35. Al-Kattan A., Nirwan V.P., Popov A., et al. *Int. J. Mol. Sci*., **19** (6), 1563 (2018).
36. Kharin A.Yu., Lysenko V.V., Rogov A., et al. *Adv. Opt. Mater*., **7** (13), 1801728 (2019).
37. Oleshchenko V.A., Kharin A.Yu., Alykova A.F., et al. *Appl. Surf. Sci*., 145661 (2020).
38. Zabotnov S.V., Skobelkina A.V., Sergeeva E.A., et al. *Sensors*, **20** (17), 4874 (2020).
39. Skobelkina A.V., Kashaev F.V., Kolchin A.V., et al. *Tech. Phys. Lett*., **46**, 687 (2020) [*Zh. Tekh. Fiz*., **46** (14), 13 (2020)].
40. Tuchin V.V. *Lasery i volokonnaya optika v biomedicinskih issledovaniyah* (Lasers and Fibre Optics in Biomedical Studies) (Moscow: Fizmatlit, 2010) p. 47.
41. Kurakina D., Khilov A., Shakhova M., Orlinskaya N., Sergeeva E., Meller A., Turchin I., Kirillin M. *J. Biomed. Opt*., **25** (6), 063804 (2019).
42. Mironycheva A.M., Kirillin M.Yu., Hilov A.V., et al. *Sovr. Tehnol. Med*., **12** (3), 47 (2020).
43. Kana E.T., Bollanti S., Di Lazzaro P., Murra D., Bouba O., Onana M.B. *Opt. Commun*., **264** (1), 187 (2006).
44. Salomatina E.V., Jiang B., Novak J., Yaroslavsky A.N. *J. Biomed. Opt*., **11** (6), 64026 (2006).
45. Roggan A., Friebel M., Doerschel K., Hahn A., Mueller G.J. *J. Biomed. Opt*., **4** (1), 36 (1999).
46. Brocato T.A., Coker E.N., Durfee P.N., Lin Y.-S., Townson J., Wyckof E.F., Cristini V., Brinker C.J., Wang Z. *Sci. Rep.,* **8**, 7538 (2018).
47. Krylov I.V., Akasov R.A., Rocheva V.V., Sholina N.V., Khochenkov D.A., Nechaev A.V., Melnikova N.V., Dmitriev A.A., Ivanov A.V., Generalova A.N., Khaydukov E.V. *Front. Chem*., **8**, 295 (2020).
48. Kirillin M.Yu., Shirmanova M.V., Sirotkina M.A., et al. *J. Biomed. Opt*., **14** (2), 21017 (2009).
49. Wang L., Jacques S.L., Zheng L. *Comput. Methods Programs Biomed*., **47** (2), 131 (1995).
50. Loginova D.A., Sergeeva E.A., Fiks I.I., Kirillin M.Yu. *J. Biomed. Photon. Eng*., **3** (1), 10303 (2017).
51. Manuchehrabadi N., Chen Y., LeBrun A., Ma R., Zhu L. *J. Biomech. Eng*., **135** (12), (2013).
52. Pennes H.H. *J. Appl. Physiol*., **1** (2), 93 (1948).
53. Ricketts P.L., Mudaliar A.V., Ellis B.E., Pullins C.A., Meyers L.A., Lanz O.I., Scott E.P., Diller T.E. *Int. J. Heat Mass Transf*., **51** (23), 5740 (2008).
54. Xu F., Lu T.J., Seffen K.A., Ng E.Y.K. *Appl. Mech. Rev*., **62** (5) (2009).
55. Bass L.P., Nikolaeva O.V., Bykov A.V., Kirillin M.Yu. *J. Biomed. Photon. Eng*., **3** (1), 10311 (2017).
56. Deng Z.-S., Liu J. *Numer. Heat Transf. Part A Appl*., **46** (6), 587 (2004).
57. Gnyawali S.C., Chen Y., Wu F., et al. *Med. Biol. Eng. Comput*., **46** (2), 159 (2008).
58. Ng E.Y.K., Tan H.M., Ooi E.H. *Burns*, **35** (7), 987 (2009).
59. Xu Y., Long S., Yang Y., Zhou F., et al. *Theor. Biol. Med. Model*., **16** (1), 1 (2019).